PHYSICAL REVIEW B **83**, 104421 (2011)

Hyperfine interactions in MnAs studied by perturbed angular correlations of γ-rays using the probe $Br^{77} \rightarrow Se^{77}$ and first-principles calculations for MnAs and other Mn pnictides

J. N. Gonçalves[*] and V. S. Amaral
Departmento de Física and CICECO, Universidade de Aveiro, P-3810-193 Aveiro, Portugal

J. G. Correia
Instituto Tecnológico e Nuclear, UFA, P-2686-953 Sacavém, Portugal

A. M. L. Lopes
Centro de Física Nuclear da Universidade de Lisboa, P-1649-003 Lisboa, Portugal

(Received 19 August 2010; revised manuscript received 22 November 2010; published 29 March 2011)

The MnAs compound shows a first-order transition at $T_C \approx 42\,^\circ$C, and a second-order transition at $T_t \approx 120\,^\circ$C. The first-order transition, with structural (hexagonal-orthorhombic), magnetic (FM-PM), and electrical conductivity changes is associated to magnetocaloric, magnetoelastic, and magnetoresistance effects. We report a study in a large temperature range from $-196\,^\circ$ up to $140\,^\circ$C, using the γ-γ perturbed angular correlations method with the radioactive probe $^{77}\mathrm{Br} \rightarrow {}^{77}\mathrm{Se}$, produced at the On-Line Isotope Mass Separator (ISOLDE)-CERN facility. The electric field gradients and magnetic hyperfine fields are determined across the first- and second-order phase transitions encompassing the pure and mixed phase regimes in cooling and heating cycles. The temperature irreversibility of the first-order phase transition is seen locally at the nanoscopic scale sensitivity of the hyperfine field, by its hysteresis, detailing and complementing information obtained with macroscopic measurements (magnetization and X-ray powder diffraction). To interpret the results hyperfine parameters were obtained with first-principles spin-polarized density functional calculations using the generalized gradient approximation with the full potential (linear) augmented plane wave plus local orbitals method (WIEN2K code) by considering the Se probe at both Mn and As sites. A clear assignment of the probe location at the As site is made and complemented with the calculated densities of states and local magnetic moments. We model electronic and magnetic properties of the chemically similar MnSb and MnBi compounds, complementing previous calculations.

DOI: 10.1103/PhysRevB.83.104421 PACS number(s): 31.30.Gs, 71.15.Mb, 75.50.Cc, 76.80.+y

I. INTRODUCTION

The magnetic compound MnAs has been intensively studied since it exhibits a magnetocaloric effect[1] under hydrostatic pressure[2] as well as when doped with metals,[1,3] making it an interesting material for magnetic refrigeration applications. Moreover, it can be grown as epitaxial films on Si and GaAs substrates[4] where applications such as a source for spin injection make it of promising use for spintronics.[5]

In parallel, it is a material with theoretical challenges. On this front, some first-principles studies are directed to this compound (see, e.g., Refs. 6–10). The orthorhombic phase is usually considered paramagnetic, however, it does not follow a Curie-Weiss law and it has also been considered to be antiferromagnetic.[8] Also of interest is the existing magnetoresistance effect which is attempted to be related to the colossal magnetoresistance (CMR) found in the perovskite manganites,[11] and is a remarkable spin-phonon coupling found crucial to the magnetostructural transition.[10] Its particular coupling of magnetism and structure has been the origin of macroscopic models[12] for magneto-volume effects.

At low temperatures, MnAs is ferromagnetic and it has a NiAs-type structure. This structure, with space group $P6_3mmc$ (194), has Mn and As atoms at coordinates (0,0,0) and (1/3, 2/3, 1/4), respectively, with two formula units per unit cell. On heating, at about $40\,^\circ$C, it undergoes a first-order phase transition, with a discontinuous distortion to the orthorhombic MnP-type structure, with a parallel discontinuous change of volume, loss of ferromagnetism, and a metal-insulator transition. The orthorhombic distortion continuously disappears when heating until about $125\,^\circ$C where it undergoes a second-order phase transition to the NiAs-type structure with a paramagnetic state, now following a Curie-Weiss law.

Thermal hysteresis is measured in this transition: on heating, the hexagonal → orthorhombic phase transformation occurs at temperatures $T_{C,i} \approx 40.5\,^\circ$–$42.5\,^\circ$C, while on cooling this transformation occurs at $T_{C,d} \approx 33.9\,^\circ$–$37.9\,^\circ$C (Refs. 13–17) (variations in different studies probably result from small differences in the stoichiometry of samples). Phase coexistence in a temperature interval of approximately $2\,^\circ$C is reported by neutron and X-ray diffraction measurements.[11,18] The orthorhombic $B31$ structure, with the space group $Pnma(62)$, has coordinates for Mn and As atoms of (0.995, 1/4, 0.223) and (0.275, 1/4, 0.918), respectively.[15]

The lattice constants of the hexagonal phase at room temperature are $a = 3.722$, $c = 5.702$ Å, and change to $a = 5.72$, $b = 3.676$, and $c = 6.379$ Å in the orthorhombic phase (with four f.u. per unit cell) at the first-order transition corresponding to a volume loss of 2%.

We report a study in this compound using the γ-γ time differential perturbed angular correlation (PAC) spectroscopy (see, e.g., Ref. 19 for details), to our knowledge the first use of this nuclear technique in the compound. Since PAC measures the combined hyperfine interactions, magnetic hyperfine field (MHF), and electric field gradient (EFG), the sensitivity of its atomic-scale measurements allows the study of the atomic environments as a function of temperature.

Other hyperfine interactions techniques have been used for the study of MnAs and related compounds in previous studies. Using Mössbauer spectroscopy with the ^{57}Fe probe at 0.25 at percent concentration, Kirchschlager *et al.*[20] detected a quadrupole splitting, which they interpreted on the basis of the motion of the probe atoms, but they did not measure the magnetic hyperfine field. Also using ^{57}Fe impurities as probes, in the related MnAs$_{1-x}$Fe$_x$ compound[21] with $x = 0.01, 0.03$, and 0.15, Abdelgadir *et al.* reported measurements involving the first-order transition at $T_{C,d} = 2\,^\circ$C (for $x = 0.01$), where they also detected an unusual dependence of the magnetic hyperfine field. Nuclear magnetic resonance (NMR) spectroscopy has also been performed at 4 K (Ref. 22), and in the range from -190° up to $38\,^\circ$C, with double signals from both Mn and As atoms, where a resonance anomaly was observed at $\approx -50\,^\circ$C as due to atoms at the domain walls.[23]

Our work studies a temperature range from 13° to 140 °C and liquid nitrogen temperature ($-196\,^\circ$C). Measurements are made in the first-order phase-transition region and above, passing the second-order phase transition (Sec. II C). The temperature range near the first-order transition is studied in more detail (Sec. II D). X-ray powder diffraction and magnetization measurements are also performed and its results are compared with PAC results.

The experimental results are complemented with density functional theory calculations of the hyperfine parameters using the full potential mixed (linear) augmented plane wave plus local orbitals [(L)APW + lo] method. To improve and complement other first-principles studies, we also show calculations of other properties and for the chemically similar manganese pnictides MnSb and MnBi.

II. EXPERIMENTS

A. Hyperfine parameters

The two quantities of interest to the physics of MnAs that can be obtained from the PAC measurements are the EFG and the MHF (B_{hf}). The EFG is measured from the hyperfine interaction between a charge distribution with nonspherical symmetry and the nuclear quadrupole moment Q. The measurement of the quadrupole interaction gives the EFG depending on the accurate knowledge of the probe's quadrupolar moment. The EFG is defined as the symmetric traceless tensor with components taken from the second spatial derivatives of the Coulomb potential at the nuclear position. In the principal axis frame of reference, the components of interest are V_{zz} and the axial symmetry parameter η, with $|V_{zz}| > |V_{yy}| \geqslant |V_{xx}|$ and $\eta = (V_{xx} - V_{yy})/V_{zz}$. The observable frequency with PAC depends on the quadrupole nuclear moment and electric field gradient in the following way:

$$\begin{aligned} \omega_\phi &= \frac{2\pi}{4I(2I-1)}\nu_Q k, \quad \text{with} \\ \nu_Q &= \frac{eQV_{zz}}{h}, \text{ for } \eta = 0, \end{aligned} \tag{1}$$

where I is the nuclear spin and $k = 6$ for the half-integer spin. ν_Q is called the "reduced frequency" of the interaction and is independent of η and I.

The MHF, arising from the dipole-dipole interaction between the nuclear magnetic moment and the magnetic moment of the extranuclear electrons, can be expressed by

$$B_{hf} = \frac{\omega_L \hbar}{g\mu_N}, \tag{2}$$

where μ_N is the nuclear magneton, g the g factor, and ω_L the observable Larmor frequency. For interpretation of the physical origin behind B_{hf}, it is usual to decompose it in four terms

$$B_{hf} = B_C + B_{\text{orb}} + B_{\text{spin}} + B_{\text{latt}}, \tag{3}$$

where B_C is the Fermi contact interaction of the electronic spin density at the nucleus with the nuclear magnetic moment, B_{orb} and B_{dip} are the contributions of the magnetic interaction due to the electronic orbital momentum and electronic spin momentum, respectively, and B_{latt} is a contribution from the other atomic orbitals in the lattice, usually negligible.

The intrinsic inhomogeneities and remaining distributions of point defects lead to the damping of the experimental PAC spectrum, which is simulated by a Lorentzian function characterized by the σ (width) parameter.

B. Experimental details and sample preparation

A mixture of radioactive isobars of mass 77, ^{77}Kr, ^{77}Br, and ^{77}Se were produced at the On-Line Isotope Mass Separator (ISOLDE) facility at CERN, and implanted at 30 keV to a dose of approximately 10^{16} atoms/m^2 in MnAs samples at room temperature. After waiting for the decay of ^{77}Kr ($t_{1/2} \approx 74$ min) for 12 h, the PAC experiments were started on the decay of ^{77}Br to ^{77}Se, after annealing as described.

One test sample was measured as implanted, but the resulting spectrum was highly attenuated due to implantation defects. Subsequently, a first annealing step at 600 °C for 200 s was done in a vacuum (5×10^{-4} mbar), followed by a fast quench to room temperature for both samples, after which the spectra substantially improved.

The γ-γ cascade of $^{77}\text{Br} \rightarrow {}^{77}\text{Se}$ is shown in Fig. 1. The hyperfine interaction is measured in the 9.56 ns, 249.8 keV, $I = 5/2$ intermediate state of the cascade, with quadrupole moment $Q = 1.1(5)b$ and magnetic moment $\mu = 1.12(3)\mu_N$ (Ref. 24).

The directional correlation of the decays is perturbed by the hyperfine interactions and the experimental anisotropy ratio function $R(t)$, which contains all of the relevant information, is expressed as a function of time t. $R(t) = \sum A_{kk} G_{kk}(t)$, where A_{kk} are the anisotropy coefficients depending on the

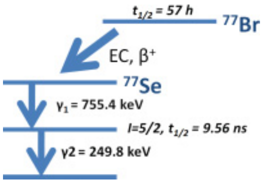

FIG. 1. (Color online) Diagram of the γ-γ decay cascade of ^{77}Se, with the properties of the relevant intermediate isotope and of the decay from the parent isotope ^{77}Br by processes of electron capture and positron emission.

spin and multipolarity of the γ decays and $G_{kk}(t)$ contains the information of the hyperfine parameters. Due to the solid angle attenuation of the detection system the anisotropy is reduced and the effective experimental anisotropy is found to be $A_{22} \approx -0.13(1)$. The long half-life of the parent isotope ^{77}Br, 57 h, and the relatively short half-life of the intermediate state allowed us to perform several measurements with a very good true to chance coincidence ratio from a single implantation shot.

The PAC spectrometer, a high efficiency setup of six BaF_2 detectors, provides 30 coincidence spectra (6 from 180° and 24 from 90° between detectors[25]).

C. First set of PAC experiments

The obtained PAC experimental functions $R(t)$ and the respective Fourier analysis are shown in Figs. 2 and 3.

The spectra are fitted using a numerical algorithm that calculates the Hamiltonian of the interaction to obtain the magnetic B_{hf} and quadrupole EFG parameters.[26] Figures 2 and 3 also show the Fourier analysis of the $R(t)$ functions for all temperatures measured.

Table I shows all fit parameters obtained at the different temperatures in the chronological order of measurements. Between the last two measurements the sample was heated to 100 °C, so the 35 °C measurement is made on cooling.

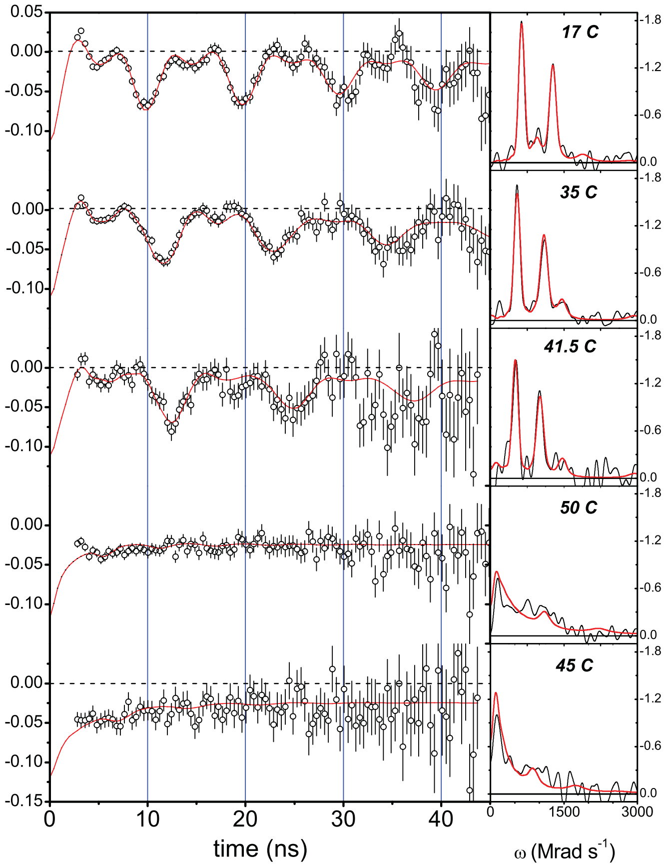

FIG. 2. (Color online) PAC spectra and Fourier transforms of the first five measurements in chronological order. The fits are represented by the red lines.

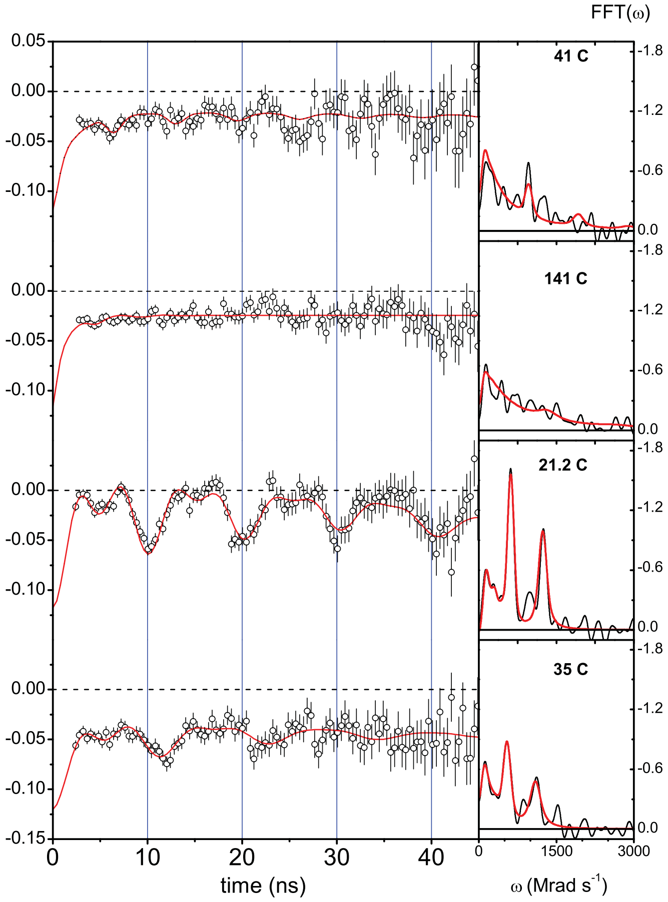

FIG. 3. (Color online) PAC spectra and Fourier transforms of the last five measurements in chronological order. Between 21.2° and 25 °C the sample was heated to 100 °C, so that the 35 °C measurement is made on cooling. The fits are represented by the red lines.

TABLE I. Fit parameters from measurements when heating and cooling the first sample, in chronological order. Fraction (%) of the measured interactions, quadrupolar frequency ω_0 (Mrad.s^{-1}), Larmor frequency ω_L (Mrad.s^{-1}), and width of Lorentzian function used in the fitting procedure σ (Mrad.s^{-1}). The magnetic frequencies have an estimated upper limit for the error of 15 Mrad.s^{-1}. The fraction f_3 and the frequency of the orthorhombic phase were kept fixed at an average value. H = hexagonal ferromagnetic, O = orthorhombic, H* = hexagonal paramagnetic.

T (°C)	f_1	ω_{L1}	σ_1	f_2	ω_{02}	σ_2	f_3	ω_{03}	σ_3	Phase
17	78	637	21	–	–	–	22	945	69	H
35	78	547	28	–	–	–	22	1466	69	
41.5	78	506	33	–	–	–	22	1484	55	
50	–	–	–	78	29	290	22	1108	10	O
45	–	–	–	78	29	330	22	874	96	
41	–	–	–	78	29	290	22	963	46	
141	–	–	–	78	29	435	22	1324	17	H*
21.2	78	618	33	–	–	–	22	176	40	H
35	60	546	65	18	28	31	22	176	43	H + O

The fit procedure can consider several fractions of ^{77}Se nuclei interacting with different hyperfine fields due to different local environments. For the ferromagnetic case the fits mainly reveal nuclei interacting with a magnetic field. Additionally for all phases, a fraction must be considered of ^{77}Se nuclei interacting with a strong (EFG$_3$) distribution that we attribute to nuclei on defect regions of MnAs which could not be annealed. This fraction was first allowed to vary, but the quality of the fit is not very sensitive to its value. In the final fits we constrained this value to the average of all previously found values, $f_3 = 22\%$.

Upon the transition the magnetic interaction vanishes and a slow frequency due to the orthorhombic phase EFG is revealed. The limited time window and low quadrupole moment makes it difficult to measure the EFG$_2$ parameters of the orthorhombic phase with high precision. Even in the most accurate measurements it can be fitted reasonably in a large range. On the other hand, the stronger EFG$_3$ of $f_3 = 22\%$ has a large damping which also makes its accurate determination difficult. Therefore in the present experiments, the asymmetry parameters η_2, η_3 were set to zero since large variations produce small changes in the results. On the other hand, this procedure agrees with the fact that the hexagonal and weakly distorted orthorhombic symmetries produce very small axial asymmetry parameters. The frequency ω_{02} was also fixed in an average value.

The magnetic phase, characterized by a well-defined magnetic hyperfine field, could be characterized also by a very small EFG. The fit program properly handles this problem by resolving the Hamiltonian for the combined interaction. In the results we present only a pure magnetic interaction since, with a combined interaction, the EFG (V_{zz}) will have to be very small in this phase and cannot be properly disentangled within the short analysis time of 45 ns. We estimate a majorant for $V_{zz} \lesssim 1 \times 10^{21}$ V/m^2, above which the quality of the fit will significantly degrade.

The obtained V_{zz} attributed to the orthorhombic phase is less than 1.1×10^{21} V/m^2 at all temperatures measured.

The frequencies ω and Lorentzian widths σ are similar for the whole temperature range in this phase. However, we point out that before the experiment, performed at 141 °C for 6 h, EFG$_2$ showed a relevant attenuation of $\sigma_2 \approx 300$ Mrads^{-1}. After this measurement the attenuation was considerably reduced and the characteristic EFG$_3$ parameters attributed to Se interacting with defects of MnAs changed considerably. Both modifications compare well with what was observed in the second set of PAC experiments immediately after the 600 °C annealing step. We think this is evidence for an incomplete annealing that was compensated for during the lengthy six-hour measurement at 141 °C.

The EFG parameters measured at 141 °C above the second-order phase transition show a very low V_{zz} as expected from the NiAs-type structure, and there is no hyperfine field since the sample should be paramagnetic, following a Curie-Weiss law at this temperature.

The measurement at 35 °C shows a lower amplitude of the $R(t)$ function due to the coexistence of hexagonal and orthorhombic phases. Still, there is a stronger attenuation of the magnetic field that can correlate with the dynamics of the phase coexistence.

The first-order transition reported in the literature when heating is clearly seen in the PAC spectra at approximately 42 °C with the disappearing magnetic hyperfine field when measuring at 50 °C.

The fact that the spectrum measured at 41.5 °C (when raising T, Fig. 2) and the spectrum measured at 41 °C (when lowering T, Fig. 3) are markedly different shows that the hysteretic behavior of the macroscopic magnetization usually measured is also present at the microscopic-local-like hyperfine field.

D. Second set of PAC experiments/first-order transition

A detailed study of the first-order transition has been done according the following order on a second sample: 21.1, 40.8, 41.3, 42.3, 43.5, 124.5 °C (raising temperature); 41.4, 39.5, 37.5, 36.6, 33.3, 32.5, 29.9, 13.3, −196 °C (lowering temperature).

The first five PAC measurements, done when heating the sample from room temperature to above the first-order transition, are shown in Fig. 4.

The five measurements, done when cooling the sample, from 36.6° to 13.3 °C, also passing the transition, are shown in Fig. 5.

The measurements done when cooling the sample above the phase transition (41.1, 39.5, 37.5, 36.5 °C), coming from a high temperature (124.5 °C), are not included since those spectra are similar to the first spectrum in Fig. 5 at 36.6 °C.

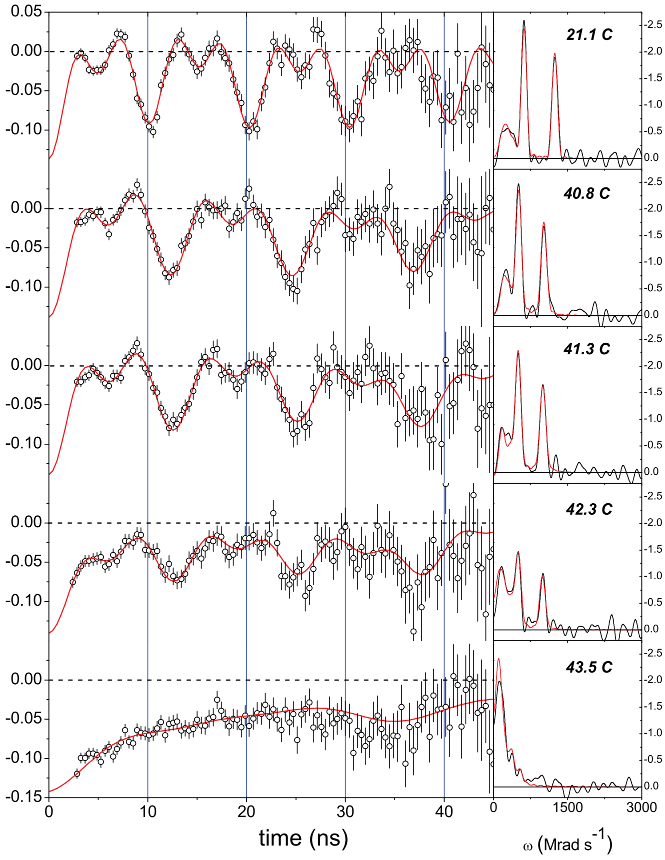

FIG. 4. (Color online) PAC spectra and Fourier transforms. Measurements made when heating the sample. The fits are represented by the red lines.

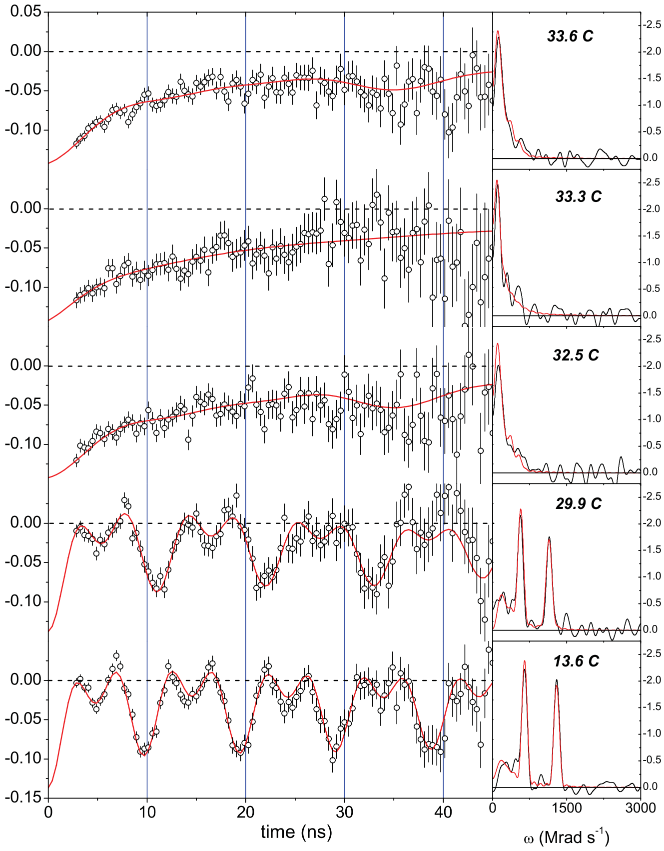

FIG. 5. (Color online) PAC spectra and Fourier transforms. Measurements made when cooling the sample. The fits are represented by the red lines.

A last measurement performed with the sample at liquid nitrogen temperature is shown in Fig. 6.

In a similar way to the preceding section, the fits were done considering a magnetic hyperfine field and low EFG, which are characteristic of each phase. For the reasons already detailed, the asymmetry parameter is set to zero for all EFG's and the fraction attributed to defect and orthorhombic frequencies are fixed in average values. Also, an additional EFG characterized by a quadrupole interaction of $\omega_0 \approx 176$ Mrad.s^{-1}, $V_{zz} \approx 6.4 \times 10^{21}$ V/m^2 is found that accounts for 30% of the probe nuclei in perturbed environments of the sample still remaining after annealing.

The values of all fitted parameters can be found in Table II.

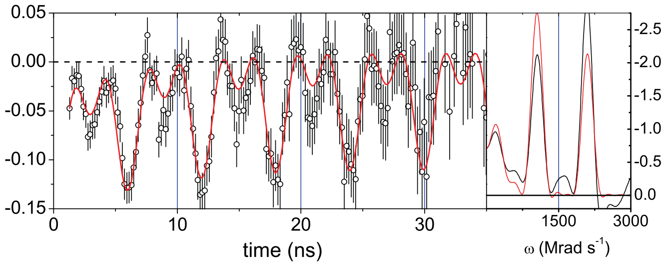

FIG. 6. (Color online) PAC spectra and Fourier transforms at −196 °C. The fits are represented by the red lines.

TABLE II. Fit parameters with temperatures in chronological order for the second sample. Fraction (%) of the measured interactions, quadrupolar frequency ω_0 (Mrad.s^{-1}), Larmor frequency ω_L (Mrad.s^{-1}), and width of Lorentzian function used in the fitting procedure σ (Mrad.s^{-1}). The magnetic frequencies have an estimated upper limit for the error of 15 Mrad.s^{-1}. f_3 and corresponding frequency were fixed at an average value as was ω_{02}. H = hexagonal ferromagnetic, O = orthorhombic.

T(°C)	f_1	ω_{L1}	σ_1	f_2	ω_{02}	σ_2	f_3	ω_{03}	σ_3	
21.1	70	619	3	–	–	–	30	176	23	
40.8	70	510	9	–	–	–	30	176	22	H
41.3	70	499	12	–	–	–	30	176	18	
42.3	40	495	10	30	28	20	30	176	10	H + O
43.5	–	–	–	70	28	24	30	176	9	
124.5	–	–	–	70	28	26	30	176	27	
41.4	–	–	–	70	28	36	30	176	17	
39.5	–	–	–	70	28	46	30	176	24	O
37.5	–	–	–	70	28	47	30	176	22	
34.5	–	–	–	70	28	29	30	176	14	
33.3	–	–	–	70	28	197	30	176	73	
32.5	–	–	–	70	28	20	30	176	11	
29.9	70	571	9	–	–	–	30	176	48	
13.6	70	648	4	–	–	–	30	176	98	H
−196	70	1050	0	–	–	–	30	57	29	

As can be seen by the changes in the spectra, the transformations occur near $T_{C,i} \approx 42.3$–$43.5°$ and $T_{C,d} = 30$–$32.6\,°$C. Therefore we estimate the thermal irreversibility to be between 10°–13.5 °C. This hysteresis is somewhat larger than that reported in other works by X-ray and magnetization measurements (10 °C).[13–17]

Figure 7 shows magnetization measurements on the same samples with a vibrating sample magnetometer with $B = 0.01$ T, showing $T_{C,i} = 45°$ and $T_{C,d} = 30.7\,°$C. The abrupt change over 2 °C, at ≈ 44 °C when heating (see Fig. 7), is in agreement with the hyperfine field changes measured above 43.5 °C.

As in the first set of PAC measurements, there is a hyperfine field of 24 T just before the transition. Then the magnetic phase disappears in a small temperature interval, as shown

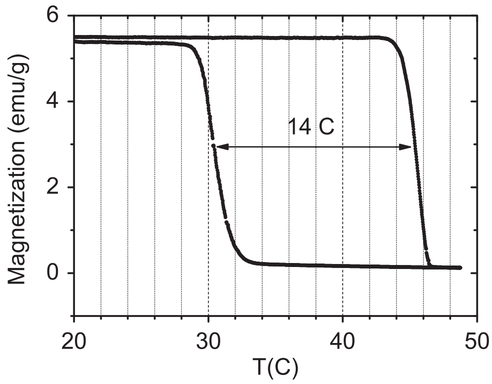

FIG. 7. Temperature dependence of the magnetization, measured at $B = 0.01$ T, signaling the strong thermal hysteresis at the first-order transition.

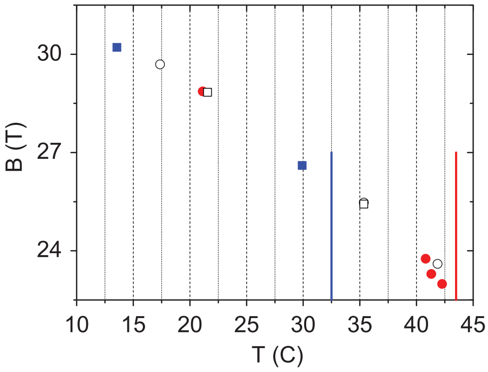

FIG. 8. (Color online) Hyperfine field of the main fraction vs. temperatures, excluding the value at −196 °C. Circles for measurements when heating, squares for cooling. The open symbols show the results of the first experiment, for comparison. The lines are the first (when heating) and last (when cooling) measurements at the orthorhombic phase.

in the spectra of Fig. 4 at 42.5° and 44.6 °C. This shows no continuous decrease of the hyperfine field to zero before the transition. Note that this conclusion cannot be learned from macroscopic magnetization measurements only (see Fig. 7), where the magnetization can be seen to decrease to zero, since just before the ferromagnetic to paramagnetic phase transition and within the temperature difference of 1 °C only a very small variation of the hyperfine field is observed. This clearly shows that the magnetization changes are mainly the result of changes in phase fractions instead of thermal disorder.

Figure 8 shows the hyperfine fields obtained where the agreement for both experiments can clearly be seen.

Notice that the attenuation of the hyperfine fields in the ferromagnetic phase increases toward the phase transition temperature. When cooling from high temperature the same behavior is observed and at liquid nitrogen temperature (−196 °C) no attenuation is observed. These observations hint at dynamic processes due to spin fluctuations.

At 42 °C the amplitude of the magnetic part of the $R(t)$ functions is smaller than at lower temperatures, showing a reduced fraction of the ferromagnetic phase still present; a fraction of 60% for the ^{77}Se atoms at the ferromagnetic phase while the other 10% show a small quadrupole frequency. This third fraction has $V_{zz} = 1.08$ (η was fixed to zero), corresponding to the value found for the other fits in the orthorhombic phase. We can say that the phase coexistence only occurs in a width of 2.2°C or less since the measurement below and at (41.3°C) and above and at (43.5°C) show only the ferromagnetic and paramagnetic phases, respectively. This width is in agreement with previous measurements of approximately 2°C (Refs. 11 and 18).

The first-order structure transformation was also probed with temperature-dependent X-ray powder diffraction studies in a Philips diffractometer. We performed detailed measurements as a function of temperature in three selected diffraction angle regions, where changes in the transition are easily seen. Three 2θ intervals were selected, 31.4°–32.6°, 41.8°–43.1°, and 48.6°–50°, where one peak characteristic of the hexagonal phase disappears in the transition with the appearance of peaks characteristic of the orthorhombic phase. In the 31.4°–32.6° 2θ interval the (101) peak disappears with the appearance of the (102) and (111) peaks almost at the same angle. The same situations occur when the (102) peak disappears and (202), (211) peaks appear in the orthorhombic phase for 41.8°–43.1°. For 48.6°–50°, the (110) hexagonal peak transforms into (013), (020), (212), and (301) peaks in the orthorhombic phase. The fit of the peaks was done simply with Gaussian functions, one Gaussian for the hexagonal peak and another Gaussian for the two or more highly overlapped orthorhombic peaks. The areas of each peak should correspond approximately to the fraction of each phase.

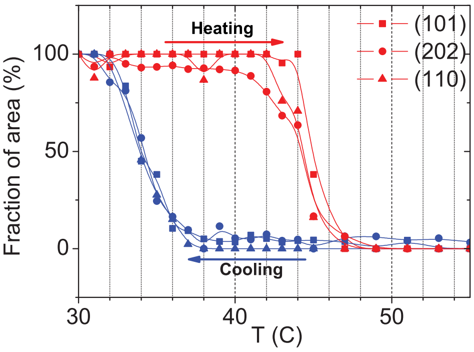

FIG. 9. (Color online) XRD fractions of the total area corresponding to the peaks of the hexagonal phase, at three 2θ intervals.

Figure 9 shows the fraction of the hexagonal phase obtained this way for the three angular intervals. The hysteresis produces here a difference of approximately 12 °C. Magnetization measurements show a somewhat higher thermal hysteresis difference at half height, 14 °C, which might indicate that the magnetic coupling is disturbed before the hysteresis is completed. The thermal hysteresis interval obtained from PAC has a large uncertainty (10°–13.5 °C), but is in agreement with both measurements.

III. FIRST-PRINCIPLES CALCULATIONS

Knowing the lattice location of the PAC probe is of fundamental importance to understanding the values obtained. After the decay of ^{77}Br, it is expected that the ^{77}Se PAC probe may be substitutional at the As site since As has a similar atomic radius and a neighbor atomic number. To check this assumption and to see the differences in the hyperfine parameters actually measured at the probe site, we have used *ab initio* density functional calculations.

Despite the existence of some published works reporting *ab initio* simulations in this system, the hyperfine parameters are usually not reported. The work of Ravindran *et al.*[9] presented the calculation of the hyperfine parameters and magneto-optical properties using density functional calculations of three manganese pnictides MnX (with X=As, Sb, and Bi). Their calculations used the full-potential linear augmented plane wave (FLAPW) method and the EFG and MHF were presented. However, as suggested by Svane,[27] the calculated structures of Ref. 9 are incorrect since the positions of Mn and the pnictide were exchanged with respect to the the stable NiAs-type structure. Recently, calculations of the hyperfine parameters in bulk and surfaces of MnAs were also reported and the correct values were obtained.[28]

TABLE III. Calculated EFG of MnAs at the hexagonal phase with room temperature lattice constants: $a = 3.722$ Å, $c = 5.702$ Å.

Atom	$V_{zz}(10^{21}\mathrm{V/m^2})$	η	V_{zz} dir.
Mn	−3.63	0	(0,0,1)
As	1.53	0	(0,0,1)

TABLE IV. Calculated hyperfine fields of MnAs (T): room temperature lattice constants: $a = 3.722$ Å, $c = 5.702$ Å, hexagonal phase.

Atom	B_C	core	valence	B_{orb}	B_{dip}
Mn	−6.5	−39.3	32.8	0.5	−3.0
As	25.0	0.4	24.5	−0.1	−0.2

Here we also calculate the hyperfine parameters with the similar full potential (L)APW + lo method, as implemented in the WIEN2K code.[29] In this method the space is divided in spheres, centered at the atoms where the valence states are described by atomic-like functions, and the interstitial space where plane waves are used.

The Mn and As atomic spheres used both have a radius of 2.5 a.u. We checked the convergency of the hyperfine parameters and total energy as a function of the number of k points used for integration in the Brillouin zone and the number of plane waves in the basis. The calculations are spin polarized and consider a ferromagnetic arrangement of Mn moments. For the calculations of hyperfine parameters, spin-orbit coupling is included, for the other properties no spin-orbit coupling is included with a scalar-relativistic basis for the valence electrons, while for the core electrons the treatment is always fully relativistic. For Mn the core states are $1s$, $2s$, $2p$, and $3s$, and the valence states are $3p$, $3d$, and $4s$, while for As $1s$, $2s$, $2p$, $3s$, and $3p$ are core states and $3d$, $4s$, and $4p$ are valence states. The Perdew-Burke-Ernzerhof (PBE) generalized gradient approximation (GGA)[30] exchange-correlation functional is used since the local spin density approximation (LSDA) is known to give poor results in this compound.[31]

The calculated EFG of the MnAs sites in the hexagonal phase is shown in Table III. Due to the hexagonal symmetry η is zero and the direction of the principal axis of the EFG tensor is parallel to the c axis. The EFG inside the spheres, which is almost equal to the total EFG, can be separated in different contributions since the the states are described in combinations of spherical harmonics with different angular momentum components. In this case the p-p and d-d contributions of the density are the dominant terms, with $V_{zz}^{pp} \propto \langle 1/r^3\rangle_p[1/2(p_x + p_y) - p_z]$ and $V_{zz}^{dd} \propto \langle 1/r^3\rangle_d[(d_{xy} + d_{x^2-y^2}) - 1/2(d_{xz} + d_{yz}) - d_{z^2}]$. For Mn, $V_{zz}^{pp} = -1.45$ and $V_{zz}^{dd} = -1.70 \times 10^{21}$ V/m^2, states where both the p and d characters contribute to the total EFG. For the As atoms, the states of the p character are the dominant contribution with $V_{zz}^{pp} = 1.27$ and $V_{zz}^{dd} = 0.06 \times 10^{21}$ V/m^2. Cutting the $3d^{10}$ states out of the density calculation the V_{zz} at As remains almost the same, confirming that the contribution from the As filled d electrons is negligible.

To improve the results of the previously mentioned work, we also calculated the EFG at MnSb and MnBi. We discuss them in Sec. IV, along with other quantities.

The Fermi contact hyperfine field at the nucleus is calculated, with the electron density averaged at a sphere with the Thomson radius $r_T = Ze^2/mc^2$, according to the formulation of Blügel *et al.*[32] in which $\overrightarrow{B}_C = \frac{8\pi}{3}\mu_B\overrightarrow{m}_{av}$ (i.e., the contact hyperfine field is parallel to the average spin density). The contributions of the contact hyperfine field due to the core and valence electron density contributions are discriminated in the tables. We remark the fact that while in As the hyperfine field is determined almost exclusively by its valence contribution, caused by the polarization by Mn atoms, the core and valence contributions of Mn cancel in a large amount. This is due to the core polarization mechanism,[32] where the core hyperfine field in Mn has a negative sign due to the polarization of core s electrons by the d shell: The majority electrons are attracted to the polarizing d electrons while the minority electrons are repelled, resulting in an excess minority charge at the nucleus. The on-site orbital and spin dipolar contributions are also calculated. These contributions are small when compared with the contact hyperfine field. To see the change due to different lattice parameters in the hyperfine fields, we also calculated with the low temperature lattice constants[33] and the obtained values are almost equal (Tables IV and V). This simply shows that the collinear spin density functional theory calculations cannot reproduce temperature related changes based only on the lattice constants.

The previously obtained hyperfine parameters are in reasonable agreement with the GGA calculations of Jamal *et al.*[28] Some differences are expected since, while their calculations consider the full theoretical lattice optimization, we only minimized the atomic forces keeping the lattice parameters fixed at the experimental values. Relative to their results, for the V_{zz} at Mn and As, small differences of 5% (1.53 against 1.46) and 4% (−3.63 against −3.78) are obtained, respectively. For the hyperfine fields the differences are −9 (present work) compared with 1 T at the As site (small absolute difference), and 24.7 (present work) compared with 31.8 T at the Mn and As sites.

To compare with the PAC results using the implanted probe, the presence of a highly diluted (*ppm*) Se probe must be accounted for in supercell calculations. The EFG and hyperfine field were calculated for hypothetical situations where the Se is substituted at As and at Mn sites using $\mathrm{Mn_{15/16}Se_{1/16}As}$ and $\mathrm{MnSe_{1/16}As_{15/16}}$ supercells.

The results for supercells with Se concentration of 1/16 are shown in Table VI. The atomic forces were not high, and were minimized by moving the free atomic coordinates. The small changes in this type of system due to the lattice constants (Tables IV and V) motivated us to keep using the MnAs room

TABLE V. Calculated contact hyperfine field of MnAs (T): low temperature lattice constants: $a = 3.732$ Å, $c = 5.678$ Å, hexagonal phase.

Atom	B_C	core	valence
Mn	−6.1	−38.7	32.5
As	25.5	0.4	35.1

TABLE VI. Hyperfine parameters with Se probe substitutional at the As or Mn sites in MnAs.

Se at As site					
$V_{zz}(10^{21}\mathrm{V/m^2})$	η	V_{zz} dir.			
−0.27	0	(0,0,1)			
B_C	core	valence	B_{orb}	B_{dip}	$-B_{hf}$ total (T)
56.6	0.4	56.2	−2.1	−0.2	54.3
Se at Mn site					
$V_{zz}(10^{21}\mathrm{V/m^2})$	η	V_{zz} dir.			
17.80	0	(0,0,1)			
B_C	core	valence	B_{orb}	B_{dip}	$-B_{hf}$ total (T)
−23.1	−22.9	−0.2	3.4	−1.8	−21.5

temperature lattice constants. The hyperfine field calculated with the Se atom substitutional at the As or Mn sites would be exact only at 0 K (disregarding zero-point effects, which should be small[34]). Our closest measured value is at liquid nitrogen.

There is a good agreement of the measured 49 T at 77 K when compared with the calculated 54.3 T at the As site. In contrast, for the case in which Se is substitutional at the Mn site, $|B_{hf}|$ is too low when compared to the experiment, even near the transition, and the very high $V_{zz} = 17.4 \times 10^{21}$ V/m^2 immediately discards the possibility that the probe is located there, whereas the EFG is very small for As-site substitutional Se, in agreement with the experiment. The calculation of the formation energies ΔH_f for the two substitutions also indicates this assignment,

$$\Delta H_f = E_{\mathrm{imp}}^{\mathrm{sup}} - 8 \times E^{\mathrm{MnAs}} - \mu_{\mathrm{Se}} + \mu_{As/Mn}, \tag{4}$$

where $E_{\mathrm{imp}}^{\mathrm{sup}}$ is the total energy of the $2 \times 2 \times 2$ supercell with a Se impurity, E^{MnAs} is the energy calculated for the pure compound, and μ_{Se} is taken as the total energy of nonmagnetic *hcp* Se. The chemical potential of As or Mn (according to the substituted site) is set as the energies of *fcc* antiferromagnetic Mn and nonmagnetic rhombohedral As. The formation energy obtained for substitution at the As site is 0.03 eV, while for the Mn substitution it has a higher value of 2.84 eV, confirming the hyperfine calculation. However, since Br is the implanted atom, if there is no time for relocation between the Br → Se decay and the PAC measurement, the formation energy of Br should be a better indication. Therefore, we also calculate these formation energies, using the energies of supercells of the same size for the same substitutions, with Br and the energy of nonmagnetic solid Br$_2$ as μ_{Br}, instead of μ_{Se}, in the previous formula. The obtained results are 0.94 eV for the Br at As substitution, and 3.95 eV at the Mn site, again confirming the As substitution.

IV. MANGANESE PNICTIDES

Full potential calculations of the hyperfine parameters and other properties of manganese pnictides were performed by Ravindran *et al.*,[9] but with the anti-NiAs structure. Here we report the same properties as calculated with the FLAPW method (i.e., the spin magnetic moments, the density of states, and the hyperfine parameters, with the NiAs-type structure).

The hyperfine parameters are especially sensitive to the type of structure. For the atoms of Mn and As, in the true structure $V_{zz} = -3.7$ and $1.4 \times 10^{21}\mathrm{V/m^2}$, respectively, while in the anti-MnAs structure $V_{zz} = 0.4$ and $11.8 \times 10^{21}\mathrm{V/m^2}$.

TABLE VII. EFG of MnAs, MnSb, and MnBi, *p*-*p* and *d*-*d* contributions in the atomic spheres.

Compound	Atom	$V_{zz}(10^{21}\mathrm{V/m^2})$	$\mathrm{V}_{zz}^{p\text{-}p}$	$\mathrm{V}_{zz}^{d\text{-}d}$
MnAs	Mn	−3.63	−1.45	−1.70
	As	1.53	1.27	0.06
MnSb	Mn	−3.92	−1.40	−1.97
	Sb	4.67	3.97	0.10
MnBi	Mn	−4.43	−1.91	−2.49
	Bi	9.46	9.44	0.21

Table VII shows the EFG of the three manganese pnictides. The asymmetry parameter and V_{zz} direction are omitted, since they are always 0 and (0,0,1). The EFG of the pnictide site increases with increasing atomic number (As, Sb, Bi), which coincidentally also happens in the work of Ravindran *et al.*[9] For the EFG of Mn the situation is reversed, in our calculations its absolute value increases, while their results with the inverted structure have a slight decrease ascribed to volume effects, which cannot be true now.

The spin moments for each atom, calculated inside the LAPW spheres, are presented in Table VIII. Experimental values and values obtained from other band-structure calculations are also presented. With our calculation, the values obtained, in μ_N per formula unit, are now in a better agreement with the experiment. Similar calculations (references in Table VIII), which have used the NiAs structure, get values which are in accordance to our results. consistently lower than the experiment.

The spin projected density of states (DOS) for the three manganese pnictides is shown in Fig. 10, with energy reference equal to the Fermi energy. The band structure has been obtained before for these compounds by several authors.

TABLE VIII. Total magnetic moment for MnX (X=P, As, Sb, Bi) in the cell and magnetic moments inside the Mn and X LAPW spheres, in units of μ_B/formula unit. Previous experiments and calculations are compared with our results.

$10^{21}\mathrm{V/m^2}$ Compound	Mn_s	X_s	MnX_t
MnAs(present work)	3.29	−0.14	3.17
MnAs(exp.)		−0.23[38]	3.40[38]
MnAs(theory)			3.10[39]
	3.14	−0.08	3.06[40]
	3.18	−0.13	3.14[28]
MnSb(present work)	3.44	−0.14	3.34
MnSb(exp.)		−0.30[38]	3.55[41]; 3.50[42]
MnSb(theory)	3.34	−0.07	3.27[39]
	3.35	−0.032	3.32[43]
	3.30	−0.06	3.24[44]
	3.5	−0.17	3.31[45]
MnBi(present work)	3.49	−0.11	3.42
MnBi(exp.)			3.82[46]; 3.84[47]; 3.9[48]
MnBi(theory)	3.71	−0.10	3.61[40]
	3.50	−0.02	3.56[49]

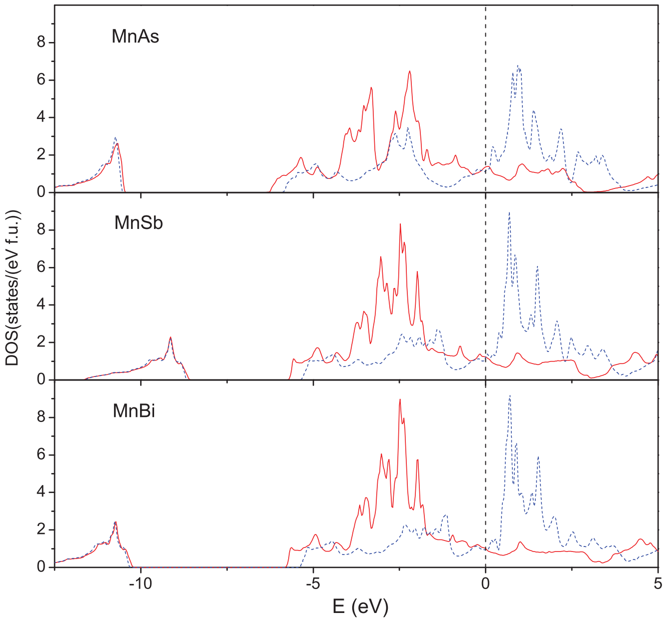

FIG. 10. (Color online) Total DOS for MnAs, MnSb, and MnBi in units of *states*/(eV *f.u.*). The up states are represented by the red solid line and the down states by the blue dashed line. Energy is in eV, relative to the Fermi energy (dashed line).

Although the DOS obtained by Ref. 9 is different, coincidentally most of the qualitative features apply also. Mainly Mn d and pnictide p states hybridize decreasing the free value $5\mu_B$. In both our study and theirs there are large peaks at the up states, below the Fermi energy, largely due to Mn d states, at approximately -2.5 eV. The Mn d states for the down spin are shifted to the conduction band. This can be seen in Fig. 11, where the important states of each atom are discriminated in their s, p, and d characters. The As s states are nearly isolated between 13 and 10.5 eV below the Fermi energy. The total number of states at the Fermi level is 2.51 for MnAs, 2.22 for MnSb, and 1.95 for MnBi. In comparison, with the antistructure the values are higher, respectively, 3.46, 2.78, 2.05,[9] which suggests that the structure is not so stable, as expected. The experimental value of 2.4 ± 0.4 states for MnSb estimated from specific heat measurements[35] is also in agreement.

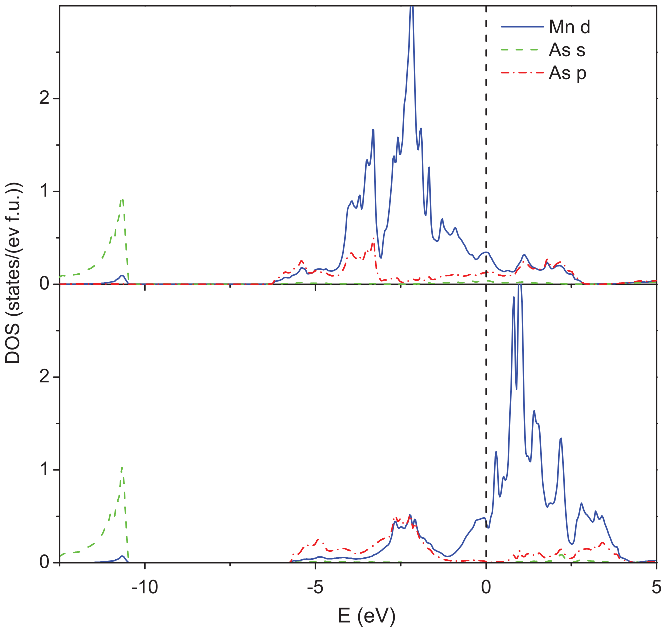

FIG. 11. (Color online) Density of states of MnAs in the hexagonal phase divided in the most important contributions for the majority (upper figure) and minority (lower figure) states.

TABLE IX. Fermi contact hyperfine fields of MnAs, MnSb, and MnBi, core and valence contributions, orbital and dipolar hyperfine fields (T).

Atom	B_C	core	valence	B_{orb}	B_{dip}
Mn	−6.5	−39.3	32.8	0.5	−3.0
As	25.0	0.4	24.6	−0.1	−0.2
Mn	−8.5	−41.5	33.0	1.2	−2.8
Sb	30.6	−2.0	30.8	0.1	−0.5
Mn	−5.8	−42.1	36.3	3.6	−2.8
Bi	82.6	−1.2	83.8	0.2	−1.0

The magnetic hyperfine field (Table IX) increases greatly from MnSb to MnBi due to the larger polarization from the s electrons at the nuclear position, which largely increases due to the additional s orbitals of higher principal atomic number, and the fact that Mn in MnBi has the larger magnetic moment, so that it polarizes the Bi valence electrons. The magnetic moment of the pnictogen site is very small, so that the core contribution of the hyperfine field is also small. For MnSb, previous NMR measurements have determined a frequency of 260 MHz at low temperatures, attributed to domain wall edge resonances,[36] corresponding to a hyperfine field $B_{hf} = 3.93$ T, equal to our calculated value for the bulk. The hyperfine field has been measured in MnBi, at the Bi atoms by nuclear orientation,[37] $B_{hf} = 94$ T, comparing reasonably with our value of 81.8 T.

V. CONCLUSION

We have measured the hyperfine parameters with the PAC method in MnAs. The hysteresis at the hexagonal-orthorhombic first-order phase transition is clearly seen from a microscopic point of view, complementing the X-ray and magnetization measurements. The hyperfine magnetic field is the same at a given temperature, irrespective of cooling or heating the sample even in the phase coexistence region. This local probe study shows that the magnetization changes observed are mostly due to a change of phase fractions, which can be related to X-ray diffraction (XRD) studies. We provide a clear demonstration of the nature of the first-order phase transition by microscopic observation of phase separation at the hyperfine interactions range (sensitive to approximately less than 10 Å), much shorter than the range of diffraction techniques. We measured phase coexistence in a small interval of temperature (2 °C), comparable with previous measurements. In contrast, in other cases PAC measurements were able to find very small coexistent regions of two competing phases, in a much broader temperature range than that given by XRD.[50]

Ab initio calculations are used to complement the experiment. Realistic simulations of the diluted probe with supercell calculations show that the ^{77}Se probe, if substitutional, is located at the As site. This information is taken from the comparison of calculated and measured hyperfine parameters, and it is verified by the calculated formation energies. Our results reproduce the hyperfine field at low temperature with good quantitative agreement.

It may be interesting to try an experiment with a probe of high quadrupole moment since, in this case, the EFG is very small and has an overlying high amplitude MHF, which makes its accurate determination difficult. Improved results for the compounds MnSb and MnBi, of hyperfine parameters, magnetic moments, and DOS were also presented and discussed.

ACKNOWLEDGMENTS

This work was supported by the Portuguese Foundation for Science and Technology FCT, with Projects No. CERN-FP-109357-2009, No. CERN-FP-109272-2009, the German BMBF funding resources and by the ISOLDE collaboration with approved Project No. IS487. J. N. Gonçalves acknowledges FCT PhD Grant No. SFRH/BD/42194/2007. The authors gratefully acknowledge S. Gama for supplying the MnAs samples, R. Soares for XRD measurements, and H. Haas for useful discussions.

---

[*] joaonsg@ua.pt

[1] H. Wada and Y. Tanabe, Appl. Phys. Lett. **79**, 3302 (2001).

[2] S. Gama, A. A. Coelho, A. de Campos, A. M. G. Carvalho, F. C. G. Gandra, P. J. von Ranke, and N. A. de Oliveira, Phys. Rev. Lett. **93**, 237202 (2004).

[3] A. de Campos, D. L. Rocco, A. M. G. Carvalho, L. Caron, A. A. Coelho, S. Gama, L. M. da Silva, F. C. G. Gandra, A. O. dos Santos, L. P. Cardoso, P. J. von Ranke, and N. A. de Oliveira, Nat. Mater. **5**, 802 (2006).

[4] L. Däweritz, Rep. Prog. Phys. **69**, 2581 (2006).

[5] M. Ramsteiner, H. Y. Hao, A. Kawaharazuka, H. J. Zhu, M. Kästner, R. Hey, L. Däweritz, H. T. Grahn, and K. H. Ploog, Phys. Rev. B **66**, 081304 (2002).

[6] L. M. Sandratskii and E. Şaşioğlu, Phys. Rev. B **74**, 214422 (2006).

[7] I. Rungger and S. Sanvito, Phys. Rev. B **74**, 024429 (2006).

[8] M. K. Niranjan, B. R. Sahu, and L. Kleinman, Phys. Rev. B **70**, 180406 (2004).

[9] P. Ravindran, A. Delin, P. James, B. Johansson, J. M. Wills, R. Ahuja, and O. Eriksson, Phys. Rev. B **59**, 15680 (1999).

[10] J. Łażewski, P. Piekarz, J. Toboła, B. Wiendlocha, P. T. Jochym, M. Sternik, and K. Parlinski, Phys. Rev. Lett. **104**, 147205 (2010).

[11] J. Mira, F. Rivadulla, J. Rivas, A. Fondado, T. Guidi, R. Caciuffo, F. Carsughi, P. G. Radaelli, and J. B. Goodenough, Phys. Rev. Lett. **90**, 097203 (2003).

[12] C. P. Bean and D. S. Rodbell, Phys. Rev. **126**, 104 (1962).

[13] J. B. Goodenough and J. A. Kafalas, Phys. Rev. **157**, 389 (1967).

[14] F. C. Nascimento, A. O. dos Santos, A. de Campos, S. Gama, and L. P. Cardoso, Mater. Res. **9**, 111 (2006).

[15] R. H. Wilson and J. S. Kasper, Acta Crystallogr. **17**, 95 (1964).

[16] F. Ishikawa, K. Koyama, K. Watanabe, and H. Wada, Jpn. J. Appl. Phys. **42**, L918 (2003).

[17] F. Ishikawa, K. Koyama, K. Watanabe, and H. Wada, Physica B: Condensed Matter **346–347**, 408 (2004), proceedings of the 7th International Symposium on Research in High Magnetic Fields.

[18] S. Gama, A. de Campos, A. A. Coelho, C. S. Alves, Y. Ren, F. Garcia, D. E. Brown, L. M. da Silva, A. M. G. Carvalho, F. C. G. Gandra, A. O. dos Santos, L. P. Cardoso, and P. J. von Ranke, Adv. Funct. Mater. **19**, 942 (2009).

[19] G. Schatz and A. Weidinger, *Nuclear Condensed Matter Physics: Nuclear Methods and Applications* (Wiley, New York, 1996).

[20] B. Kirchschlager, H. Berg, and K. Bärner, Phys. Lett. **82**, 46 (1981).

[21] M. A. Abdelgadir, L. Häggström, T. Sundqvist, and H. Fjellvåg, Phys. Scr. **37**, 373 (1988).

[22] Y. Amako, H. Nagai, and H. Ido, J. Magn. Magn. Mater. **272–276**, E1617 (2004).

[23] S. Pinjare and K. Rama Rao, J. Magn. Magn. Mater. **30**, 27 (1982).

[24] N. Stone, At. Data Nucl. Data Tables **90**, 75 (2005).

[25] T. Butz, S. Saibene, T. Fraenzke, and M. Weber, Nuclear Instruments and Methods in Physics Research Section A: Accelerators, Spectrometers, Detectors and Associated Equipment **284**, 417 (1989).

[26] N. P. Barradas, M. Rots, A. A. Melo, and J. C. Soares, Phys. Rev. B **47**, 8763 (1993).

[27] A. Svane, Phys. Rev. B **68**, 064422 (2003).

[28] M. Jamal, S. Javad Hashemifar, and H. Akbarzadeh, J. Magn. Magn. Mater. **322**, 3841 (2010).

[29] P. Blaha, K. Schwarz, G. K. H. Madsen, D. Kvasnicka, and J. Luitz, WIEN2K—An Augmented Plane Wave + Local Orbitals Program for Calculating Crystal Properties; www.wien2k.at.

[30] J. P. Perdew, K. Burke, and M. Ernzerhof, Phys. Rev. Lett. **77**, 3865 (1996).

[31] Y.-J. Zhao, W. T. Geng, A. J. Freeman, and B. Delley, Phys. Rev. B **65**, 113202 (2002).

[32] S. Blügel, H. Akai, R. Zeller, and P. H. Dederichs, Phys. Rev. B **35**, 3271 (1987).

[33] T. Suzuki and H. Ido, J. Phys. Soc. Jpn. **51**, 3149 (1982).

[34] D. Torumba, K. Parlinski, M. Rots, and S. Cottenier, Phys. Rev. B **74**, 144304 (2006).

[35] K. Liang and T. Chen, Solid State Commun. **23**, 975 (1977).

[36] C. Narasimha Rao, J. Magn. Magn. Mater. **50**, 107 (1985).

[37] H. Koyama, K. Nagamine, N. Nishida, K. Tanaka, and T. Yamazaki, Hyperfine Interact. **5**, 27 (1977).

[38] Y. Yamaguchi and H. Watanabe, J. Magn. Magn. Mater. **31–34**, 619 (1983).

[39] K. Katoh, A. Yanase, and K. Motizuki, J. Magn. Magn. Mater. **54–57**, 959 (1986)

[40] P. M. Oppeneer, V. N. Antonov, T. Kraft, H. Eschrig, A. N. Yaresko, and A. Y. Perlov, J. Appl. Phys. **80**, 1099 (1996).

[41] J. Bouwma, C. van Bruggen, C. Haas, and B. Van Laar, Physica, 78 (1971).

[42] T. Chen, G. B. Charlan, and R. C. Keezer, J. Cryst. Growth **37**, 29 (1977).

[43] N. Vast, B. Siberchicot, and P. G. Zerah, J. Phys. Condens. Matter **4**, 10469 (1992).

[44] R. Coehoorn, C. Haas, and R. A. de Groot, Phys. Rev. B **31**, 1980 (1985).

[45] R. Podloucky, Solid State Commun. **50**, 763 (1984).

[46] L. Zhiqiang, L. Helie, L. Wuyan, Z. Zhi, and Z. Qingqi, Solid State Commun. **79**, 791 (1991).

[47] T. Chen and W. Stutius, Magnetics, IEEE Transactions on **10** (1974).

[48] R. R. Heikes, Phys. Rev. **99**, 446 (1955).

[49] J. Köhler and J. Kübler, Physica B: Condensed Matter **237–238**, 402 (1997).

[50] A. M. L. Lopes, J. P. Araújo, J. J. Ramasco, V. S. Amaral, R. Suryanarayanan, and J. G. Correia, Phys. Rev. B **73**, 100408 (2006).